



Secondary Infall in the Seyfert's Sextet: A Plausible Way Out of the Short Crossing Time Paradox

Omar López-Cruz^{1,10}, Héctor Javier Ibarra-Medel^{2,3}, Sebastián F. Sánchez³, Mark Birkinshaw⁴, Christopher Añorve⁵,
Jorge K. Barrera-Ballesteros³, Jesús Falcon-Barroso^{6,7}, Wayne A. Barkhouse⁸, and Juan P. Torres-Papaqui⁹

¹Coordinación de Astrofísica, Instituto Nacional de Astrofísica Óptica y Electrónica (INAOE), Luis E. Erro No. 1, Sta. Ma. Tonantzintla, Puebla, C.P. 72840, México; omarlx@inaoep.mx

²University of Illinois Urbana-Champaign, Department of Astronomy, 103 Astronomy Building, 1002 W Green Street, Urbana, IL 61801, USA

³Instituto de Astronomía, Universidad Nacional Autónoma de México (IA-UNAM), Cd. de México, México

⁴HH Wills Physics Laboratory, University of Bristol, Tyndall Avenue, Bristol, BS8 1TL, UK

⁵Facultad de Ciencias de la Tierra y el Espacio (FACITE), Universidad Autónoma de Sinaloa (UAS), Culiacán, Sinaloa, México

⁶Instituto de Astrofísica de Canarias, Calle Vía Láctea s/n, E-38205, España

⁷Departamento de Astrofísica, Universidad de La Laguna (ULL), E-38200 La Laguna, Tenerife, España

⁸Department of Physics and Astrophysics, University of North Dakota, Grand Forks, ND 58202, USA

⁹Departamento de Astronomía, Universidad de Guanajuato (DAUG), Callejón Jalisco s/n Col. Valenciana, Guanajuato, C.P. 36240, México

Received 2019 April 11; revised 2019 October 16; accepted 2019 October 23; published 2019 November 13

Abstract

We used integral field spectroscopy from CALIFA DR3 and multiwavelength publicly available data to investigate the star formation histories of galaxies in the Seyfert's Sextet (SS; HCG 79). The galaxies H79a, H79b, H79c, and H79f have low star formation rates despite showing strong signs of interaction. By exploring their individual specific star formation histories, we identified three earlier episodes of strong star formation common to these four galaxies. We use the last two episodes as markers of the epochs when the galaxies were crossing. We suggest that after the first turnaround, initially gas-rich galaxies crossed for the first time, consuming most of their gas. Hence, after the second turnaround most mergers from second crossings would be mixed or dry. The exception would be gas-rich galaxies intruding for the first time. Therefore, we suggest that SS galaxies have survived one crossing during a Hubble time. Strong Balmer absorption lines and the presence of counter-rotating disks provide independent bounds to the second and first crossing, respectively. This scenario provides a plausible way out of the short crossing time paradox.

Unified Astronomy Thesaurus concepts: [Star formation \(1569\)](#); [Stellar evolution \(1599\)](#); [Disk galaxies \(391\)](#); [E+A galaxies \(424\)](#); [Stellar evolutionary models \(2046\)](#); [Galaxy dynamics \(591\)](#); [Galaxies \(573\)](#); [Galaxy collisions \(585\)](#); [Galaxy mergers \(608\)](#); [Galaxy groups \(597\)](#); [Galactic and extragalactic astronomy \(563\)](#); [Hickson compact group \(729\)](#)

1. Introduction

For quite some time, it has been known that the crossing times ($t_c \sim D/\sigma$, where D is the group's diameter and σ is the velocity dispersion) in compact groups (CGs) are much shorter than the Hubble time, $t_H = 12.6 h_{75}^{-1} \text{Gyr}$ (e.g., Hickson 1993). For example, Diaferio et al. (1993) used observations and numerical simulations to find that $t_c \sim 0.13 t_H$. This, along with similar previous results, has led to the so-called short dynamical time paradox (e.g., White 1990; Diaferio et al. 1993; Barnes 1997). Naively, one would expect that most CGs should have already collapsed into a single merger remnant, resembling, perhaps, a giant early-type galaxy. Many scenarios have been proposed as ways out of this apparent paradox. Here, we consider the three most common scenarios:

1. CGs are chance projections along the line of sight;
2. CGs have just assembled; and
3. galaxies in CGs have survived many crossings.

Scenario 2 is complementary to the replenishing scenario proposed by Diaferio et al. (1993). Below, we argue in favor of the third scenario. We propose that CGs have collapsed at least

once during a Hubble time; nonetheless, some group galaxies survived intact.

We have revisited Seyfert's Sextet (SS, HCG 79; Seyfert 1951), a much-studied CG (e.g., Peebles 1971; Durbala et al. 2008). The galaxies H79a, H79b, H79c, H79d, and H79f (also a galaxy; see Section 4.1) are members of SS, while H79e ($z = 0.06$) is a background galaxy. The naming of the galaxies follows Hickson (1993) and Durbala et al. (2008, hereafter Du08). SS was singled out by Peebles (1971), remarking on its high galaxy density and short dynamical time. Peebles went further by suggesting that spiral galaxies would be short-lived in CG environments. We can use Sloan Digital Sky Survey (SDSS) data to show that SS is an isolated group (e.g., Díaz-Giménez & Zandivarez 2015); hence, it is an excellent site to investigate how its spiral galaxies have survived.

In this Letter, we present an analysis of integral field spectroscopy (IFS) observations from the Calar Alto Legacy Integral Field Area Survey Data Release 3 (CALIFA DR3; Sánchez et al. 2016), supplemented with archival data from *Hubble Space Telescope* (HST), SDSS, *Spitzer*, *Herschel*, and *Wide-field Infrared Survey Explorer* (WISE) (Section 2). We have considered the fossil stellar record (Section 2.3) of galaxies and secondary infall (see Section 3) to develop a simple timing argument (Section 4.1). The state of the gas, dust, and galactic activity and dynamics of SS galaxies is

¹⁰ 2015–2016 Oliver L. Benediktson Endowed Chair in Astrophysics, Department of Physics and Astrophysics, University of North Dakota, Grand Forks, ND 58202, USA.

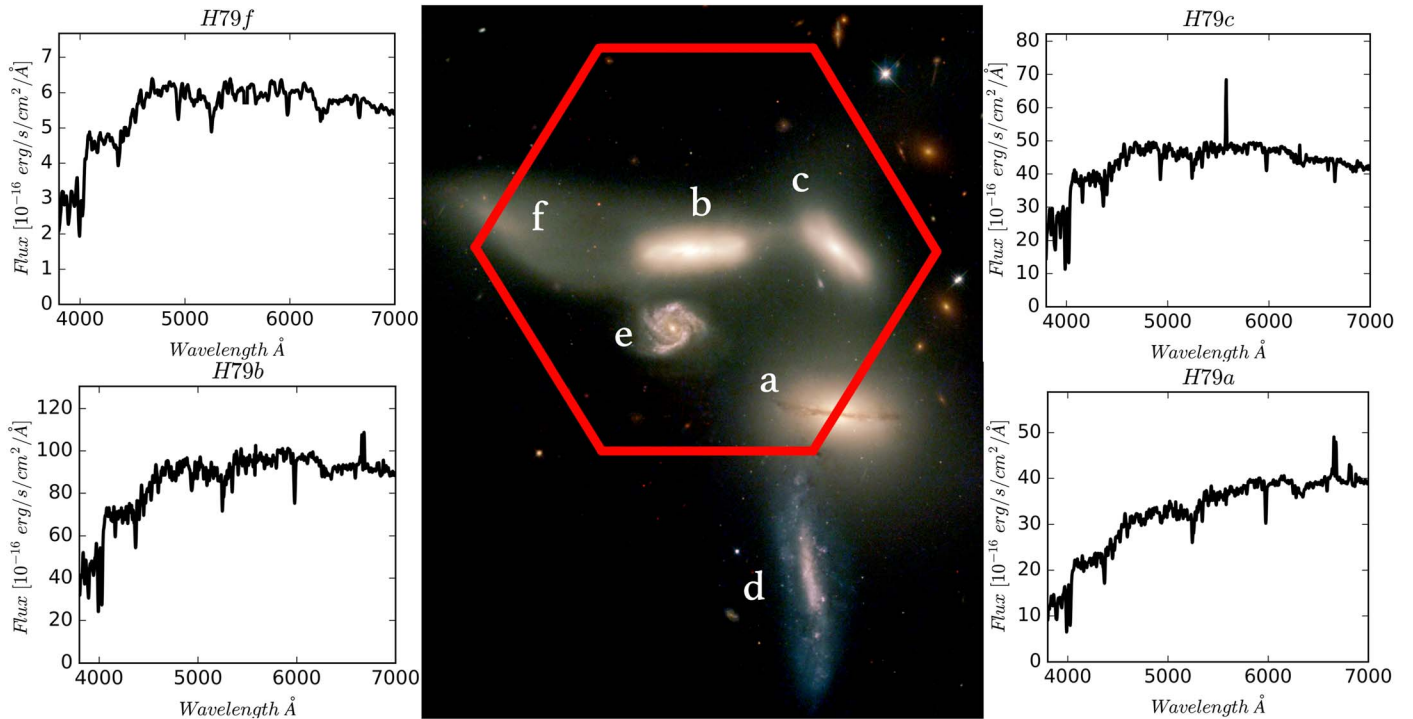


Figure 1. CALIFA’s footprint, indicated by the red hexagon, on an *HST* composite image of Seyfert’s Sextet, with the spectra of galaxies H79a, H79b, H79c, and H79f integrated down to $1.5 \times$ the effective radius, R_e . Spiral galaxy H79d is also a member of this CG, but was missed by this *HST* pointing. H79e is a background galaxy. The wavelength axis (Å) is indicated, while the spectral flux is in units of $10^{-16} \text{ erg s}^{-1} \text{ cm}^{-2} \text{ Å}^{-1}$. The 4000 Å break and the absorption lines Mg β λ 5175 and NaD λ 5892 are clearly seen. Emission in H α is seen in H79a and H79b. H β is seen in H79c. The color was composed from WFPC2 images using the filters F336W, F439W, F555W, and F814W—see <https://hubblesite.org/image/1242/gallery> for further details.

presented in (Section 4) to establish the evolutionary stage of Seyfert’s Sextet. Finally in Section 5, we compare the three scenarios presented above, and summarize the results and inferences drawn from this study.

We assumed $H_0 = 75 h_{75} \text{ km s}^{-1} \text{ Mpc}^{-1}$, $\Omega_m = 0.3$, and $\Omega_\Lambda = 0.7$ throughout this Letter, to allow direct comparisons with previous works.

2. Observations and Analysis Techniques

2.1. CALIFA DR3 Observations

CALIFA DR3 contains IFS data cubes for 939 low- z ($0.005 < z < 0.03$) galaxies, selected by diameter (Sánchez et al. 2016). The data were taken with the Calar Alto Observatory’s 3.5 m telescope and the Potsdam Multi-Aperture Spectrophotometer (Roth et al. 2005), using the PPAK (Kelz et al. 2006) integral field unit (IFU) mode. This mode covers a hexagonal field of view (FOV) of $74'' \times 62''$ ($1.3 \square'$) with 331 fiber spectra, each of diameter $\varnothing_{\text{fiber}} = 2''7$ on the sky, while the median seeing at Calar Alto is around $1''$. We report V500 grating observations, covering 3745–7500 Å, with spectral resolution $\lambda/\Delta\lambda \sim 850$, and spatial resolution $2''5$. Three dithered 900 s integrations were taken per target galaxy, using a pattern of offsets (0, 0), (−5.22, −4.53), and (−5.22, 4.53) arcsec in (x, y) relative to the nominal position of the target. This strategy permits a 100% filling factor across the FOV. The fluxes per fiber were initially calibrated by observing standard stars with some early-type galaxies defined as secondary standards, taking account of information on observatory sky conditions (García-Benito et al. 2015; Sánchez et al. 2016). The registration procedure is described in full by García-Benito et al. (2015). The three dithered exposures were

combined in a single frame containing all 993 spectra. Sky-subtracted SDSS DR7 images were used to recalibrate the fibers using the corresponding fluxes for 331 apertures on the image of the target galaxy. The apertures were shifted by R.A. and decl. inside a search box centered on the galaxy of interest, with the best registration determined by minimizing χ^2 for the differences between the spectra of the raw stack and the SDSS aperture-matched fluxes. An accuracy of ~ 0.2 on the fiber positions was obtained and the CALIFA spectrophotometry was anchored to SDSS DR7. After Galactic extinction correction using the Schlegel et al. (1998) and Cardelli et al. (1989) prescriptions and correcting for differential atmospheric refraction, spectra were rearranged using a flux-conserving inverse-distance weighting scheme to generate the final data cubes (García-Benito et al. 2015). Further details of data selection, observational strategy, data reduction, and data products can be found in Sánchez et al. (2016) and CALIFA DR3.¹¹

The observations reported in this Letter come from a data cube centered on H79b (NGC 6027). However, due the extreme compactness of SS, four additional galaxies fell within the PPAK FOV. The 3σ detection limit per spaxel and spectral resolution element is $I_3 = 1.3 \times 10^{-18} \text{ erg s}^{-1} \text{ cm}^2 \text{ Å}^{-1} \text{ arcsec}^{-2}$ in the median at 5635 Å, resulting in a limiting surface brightness of $\mu_r = 23.4 \text{ mag arcsec}^{-2}$ (3σ). The overall spectrophotometric calibration accuracy is better than 5%. We used pipeline PIPE3D (Sánchez et al. 2016a, 2016b) for data manipulation,

¹¹ http://www.caha.es/CALIFA/public_html/?q=content/califa-3rd-data-release

masking, spectral extraction, and to estimate the star formation history (SFH).

Figure 1 shows CALIFA’s footprint on SS. About half of H79a is covered by the CALIFA pointing, barely including the nuclear regions. H79b and H79c are completely covered, while more than three-quarters of H79f are covered. The late-type H79d lies outside this CALIFA data cube. Spectra of the galaxies integrated to $1.5R_e$ (see Section 2.2) are also shown. These spectra resemble early-type galaxies: the 4000 Å break is clear and the Mgb $\lambda 5175$ and NaD $\lambda 5892$ absorption lines are also seen. Emission in H α is seen in H79a and H79b, and in H β in H79c. Figure 2(b) shows emission maps of H α for H79a, H79b, and H79c.

2.2. 2D Surface Brightness

A flux-calibrated, 2000 s integration image taken with *HST*/WFPC2 ($0''.1$ pixel $^{-1}$) in the F814W¹² band was used. We use the 2D parametric code GALFIT (Peng et al. 2010) to model the surface brightness distribution of SS galaxies. We have used the sum of one or two Sérsic models, plus an exponential disk to account for bulge, bar, and disk components, respectively. A point-spread function (PSF) generated by Tiny Tim¹³ was employed in this study. GALFIT convolves the analytical models (a surface of a single orientation, which defines the position angle) with the PSF and performs a χ^2 minimization between the convolved model and pixels on the galaxy image. See the GALFIT¹⁴ home page for further details. WFPC2 is a four CCD mosaic; to cover the gaps between CCDs, multiple shifted images are taken and then combined. Four 500 s images were DRIZZLED¹⁵ to generate the image that we used, but some gaps with small negative counts remained. Gaps and galaxy dust lanes were masked.

Diffuse intragroup light (e.g., Da Rocha & Mendes de Oliveira 2005 Du08), crowding, and tidally induced asymmetries complicate the modeling of the surface brightness. Hence, we proceeded interactively, galaxy by galaxy, considering regions of increasing sizes. In a second pass, all the galaxies were modeled simultaneously, using the previous fits as inputs. The entries in Table 1 are average parameters; the errors represent the dispersion for each parameter. Using the largest effective radius, R_e , of the fitted components for each galaxy, we consider the following regions: inner ($0.0R_e < R < 0.5R_e$), intermediate ($0.5R_e < R < 1.0R_e$), and outer ($1.0R_e < R < 1.5R_e$); see Figure 2(a). These regions will be used in further analysis below.

2.3. Fossil Stellar Record

Among the many packages and pipelines that are available to recover the fossil stellar record from the spectral energy distributions (SEDs) of galaxies¹⁶ (e.g., reviews by Walcher et al. 2011; Conroy 2013), we chose PIPE3D¹⁷ (Sánchez et al. 2016a, 2016b). This pipeline performs a set of complex operations on the input data, and uses the inversion method.

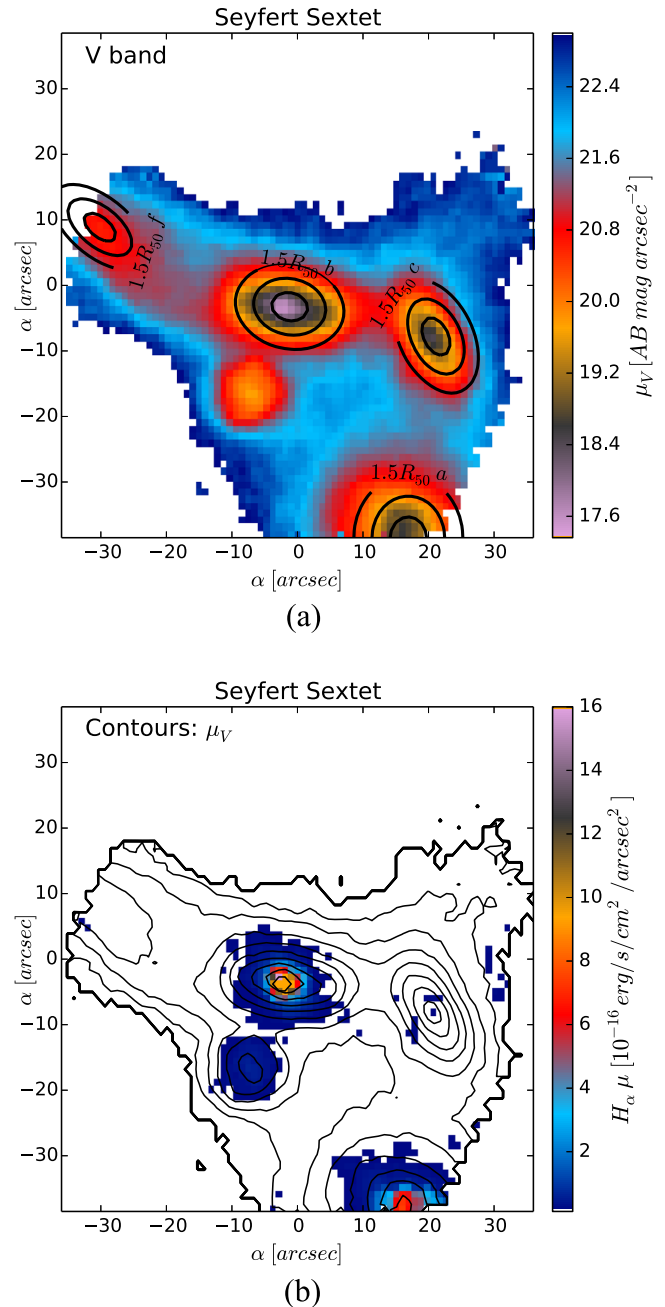


Figure 2. (a) Surface brightness distribution for SS galaxies. The ellipses delimit the inner ($0.0R_e < R < 0.5R_e$), intermediate ($0.5R_e < R < 1.0R_e$), and outer ($1.0R_e < R < 1.5R_e$) regions of interest as multiples of the projected effective radius, R_e . See Sections 2.2 and 2.3 for further details. (b) $3''$ /spaxel resolution map of the H α emission overlaid on V-band contours (black continuous lines) covering the galaxies and intragroup light. Coordinates are referred to H79b. The outermost contour indicates an isophote with $\mu_V = 23$ mag arcsec $^{-2}$. Contours are spaced in steps of $\mu_\Delta = 0.6$ mag arcsec $^{-2}$. The flux scale is indicated in color, above a lower limit of 1.2×10^{-16} erg s $^{-1}$ cm $^{-2}$ arcsec $^{-2}$.

The steps within PIPE3D are broadly described below: for further details the reader is referred to Ibarra-Medel et al. (2016, 2019) and Sánchez et al. (2016a, 2016b, 2019).

The first function of PIPE3D applies spatial binning, when necessary, to reach the minimum signal-to-noise ratio (S/N) needed to extract a realistic decomposition of the stellar population (Sánchez et al. 2016a). Then corrections are applied to account for stellar kinematics and dust attenuation for each

¹² Hubble Legacy Archive, which is a collaboration between STScI/NASA, ST-ECF/ESA, and CADC/NRC/CSA; <https://hla.stsci.edu> and <http://www.stsci.edu/hst/wfpc2>.

¹³ <http://www.stsci.edu/software/tinytim/>

¹⁴ <https://users.obs.carnegiescience.edu/peng/work/galfit/galfit.html>

¹⁵ <http://www.stsci.edu/scientific-community/software/drizzlepac.html>

¹⁶ <http://www.sedfitting.org/Fitting.html>

¹⁷ <http://www.astroscu.unam.mx/~sfsanchez/FIT3D/>

Table 1
Surface Brightness Parameter for Seyfert’s Sextet Galaxies

Galaxy	Model	r_e ($''$)	R_e (kpc)	n	e	P.A. ($^\circ$)	m (mag.)	B/T	m_T (mag.)
H79a	Sérsic	8.3 ± 0.7	2.3 ± 0.2	3.5 ± 0.2	0.325 ± 0.005	72.0 ± 0.5	13.81 ± 0.06		
-	Disk ^a	15.7	0.85	13.63
H79b	Sérsic	6.7 ± 0.6	1.8 ± 0.2	1.6 ± 0.3	0.73 ± 0.00	82.13 ± 0.08	14.2 ± 0.1		
	Exp. Disk	0.75 ± 0.06^b	0.21 ± 0.02	...	0.52 ± 0.05	74.00 ± 0.03	16.8 ± 0.2	0.92	14.12
H79c (bulge)	Sérsic	0.24 ± 0.02	0.07 ± 0.01	1.8 ± 0.1	0.14 ± 0.01	34 ± 5	20.41 ± 0.08		
- (bar)	Sérsic	1.05 ± 0.01	0.290 ± 0.003	0.5 ± 0.0	0.545 ± 0.005	33 ± 1	18.32 ± 0.03		
-	Exp. Disk	5.67 ± 0.07^b	1.56 ± 0.02	...	0.61 ± 0.01	35 ± 1	15.37 ± 0.01	0.07	15.29
H79f	Sérsic	9.1 ± 1.1	2.5 ± 0.3	0.53 ± 0.01	0.47 ± 0.01	57 ± 5	16.0 ± 0.1	...	16.0

Notes. Columns—1: name of the galaxy, 2: model fit, 3: effective radius (arcsec), 4: effective radius (kpc), 5: Sérsic index, 6: ellipticity, 7: position angle (deg), 8: integrated magnitude of each component, 9: bulge-to-total ratio, 10: apparent total magnitude.

^a No fit for the disk component was possible, light was integrated on the residual image.

^b For exponential disk fits, we report $r_e = 1.678r_h$, where r_h is the disk scale length.

(possibly spatially binned) spectrum. A limited single-stellar-population (SSP) template library is used to limit and partially avoid the degeneracies from dust, metallicity, age, and velocity dispersion. This fitting involves a nonlinear minimization (for dust and kinematics properties), and a linear fit for the combination of the dust-obscured, velocity-shifted, and broadened version of the SSP templates. The kinematics and stellar dust attenuation parameters are then fixed for the rest of the analysis. Linear fitting is repeated using an extended SSP library.¹⁸ During a first iteration the emission line regions are masked, to minimize their potential effect on the fit. A first model for the stellar population is then generated and removed from the original data to create a “pure gas” (plus noise) spectrum. The emission lines are then fitted by a set of Gaussians, and the resulting emission model is removed from the original spectrum, creating a “pure stellar population” spectrum that it is then fitted again with the SSP library. The process is repeated until convergence is reached (normally after three iterations).

Errors for each fitted parameter are estimated using Monte Carlo (MC) simulations of the original spectrum. These take into account dust attenuation of the stellar population, the velocity and velocity dispersion, the flux intensity, the velocity and velocity dispersion of the considered emission lines, and the weights of the decomposition of the stellar population in the SSP library. The process is repeated in its entirety 30 times. Using the SSP library weights, we derive the mass assembly history (MAH) following the procedure described in Sánchez et al. (2016b, 2019). First, we multiply the weight of each SSP, normalized to a predefined wavelength, by the flux intensity at that wavelength, and the mass-to-light ratio of that SSP. This give us the distribution of masses at each age and metallicity. Then we sum the masses at each age to create the cumulative function (correcting for the mass loss; following Courteau et al. 2014), i.e., the MAH. We assume that mass variations are due to star formation. Hence, by calculating the differential mass at a given epoch (defined by the age sampling in the SSPs) and dividing by the time interval, we obtain the star formation rate (SFR) at each epoch (Ibarra-Medel et al. 2019; Sánchez et al. 2019). Using this information, we can generate the SFH. Dividing the SFR by the assembled mass at each time, we obtain the specific star formation history (sSFH). This

definition is employed throughout this Letter. Errors are propagated from the MC process described above.

Comparisons with other codes and simulations have been used to validate PIPE3D, as detailed by Ibarra-Medel et al. (2016, 2019) and Sánchez et al. (2016a, 2019). For $S/N > 50$, A_V is recovered with an accuracy of about 0.06 mag and a precision of about 0.17 mag. A more important error arises from galaxy inclination (Ibarra-Medel et al. 2019). In our case, due to the distorted morphologies of the SS galaxies, it is difficult to assess the inclination realistically, so that it is difficult to estimate the magnitude of the consequent error. On the other hand, the metallicity evolution of galaxies has not been checked in detail within PIPE3D. Nevertheless, Sánchez et al. (2016a) showed that PIPE3D closely matches the results of STARLIGHT (Cid Fernandes et al. 2005). We therefore expect that PIPE3D can reproduce STARLIGHT’s chemical evolution results. A general pattern of stellar populations having lower metallicity in the past than the present is expected to emerge, but we also expect the stellar metallicity to be closely related to the stellar mass in spheroidal galaxies, but rather to stellar surface mass density in disk-dominated galaxies (e.g., González Delgado et al. 2014; Cid Fernandes et al. 2015).

We have evaluated the SFHs per spaxel using PIPE3D. Our template library contains 156 spectra to cover 39 stellar ages, from 1 Myr to 14.2 Gyr, and four metallicities ($Z/Z_\odot = 0.2, 0.4, 1.0, \text{ and } 1.5$). PIPE3D processed galaxies from SS and the control sample via brute-force fitting, exploring in fine steps all possible linear combinations of the library spectra, to obtain the best fit with no assumptions on the shape or functional form of the SFHs. The radial structure of the sSFHs (e.g., Pérez et al. 2013) is generated by an implementation by Ibarra-Medel et al. (2016) based on inner, intermediate, and outer regions as shown in Figure 1(b) (see Section 2.2 and Table 1). On average, the inner regions of galaxies H79a, H79b, and H79c have $S/N \sim 200$, and the outer regions have $S/N \sim 50$. H79f has $S/N \sim 50\text{--}60$ across the region covered.

2.4. Kinematics as Traced by Stars and Ionized Gas in Galaxy H79b

The data for H79b have high S/N , and H79b is completely covered by the CALIFA footprint. A separate analysis was performed to retrieve kinematic information following the technique described by Barrera-Ballesteros et al. (2014) and García-Lorenzo et al. (2015). On the first pass, spaxels are

¹⁸ The full SSP library is held at <https://svn.sdss.org/public/data/manga/pipe3d/trunk/data/BASE.gsd01>.

Table 2
Infrared Properties for Galaxies in the Seyfert’s Sextet Modeled Using `cmcirSED` (Casey 2012)

Galaxy	β	α	$\log L_{\text{IR}}$ (L_{\odot})	$\log M_{\text{dust}}$ (M_{\odot})	T_{dust} (K)
H79a	2.0 ± 0.0	1.61 ± 0.04	9.57 ± 0.04	6.59 ± 0.06	22 ± 1
H79b	2.3 ± 0.6	2.0 ± 0.1	9.5 ± 0.1	5.1 ± 0.1	25 ± 2
H79c	0.6 ± 0.4	3.6 ± 0.3	8.6 ± 0.1	5.1 ± 0.1	28 ± 3

Note. Columns—1: name of the galaxy, 2: emissivity, 3: mid-IR power-law slope, 4: infrared luminosity (L_{\odot}), 5: dust mass (M_{\odot}), 6: dust temperature (K).

Voronoi-binned, ignoring spaxels with $S/N < 3$, producing voxels, discrete regions where $S/N \geq 20$. To derive the line-of-sight velocity maps, each voxel is fitted, avoiding emission lines, using pPXF (Cappellari & Emsellem 2004). Errors per spaxel are estimated via MC simulations and range from 5 to 20 km s^{-1} (Barrera-Ballesteros et al. 2014). Ionized-gas maps are generated after the stellar contribution is removed. The velocities are derived using the cross-correlation method implemented by García-Lorenzo et al. (2015). Each spectrum (whose $S/N > 8$) is compared with a template that includes the $H_{\alpha} + [\text{N II}] \lambda\lambda 6548, 6684$ emission lines in the interval $6508\text{--}6623 \text{ \AA}$. Templates are convolved with Gaussians to account for the instrumental resolution and shifted to the galaxy systematic velocity. Typical errors in the velocities are of the order of 10 km s^{-1} . Stellar and ionized-gas velocity maps are shown in Figure 5(a).

2.5. Dust Properties

We used an independent indicator of star formation to check the results from Section 2.3. Although a more detailed analysis has been provided by Bitsakis et al. (2011, 2014), we wanted to compare the results from a simple but robust method using additional data. We applied the code `cmcirSED` developed by Casey (2012) to model the IR SED in wavelength range $8\text{--}500 \mu\text{m}$, generated from *Spitzer*, *WISE*, and *Herschel* data. `cmcirSED` fits these data with a modified single-temperature graybody plus a power law. We performed the fit for H79a, H79b, and H79c. After allowing the emissivity index (β) and the mid-IR power-law slope (α) to vary, we derived the peak wavelength dust temperature T_{dust} , the infrared luminosity integrated from $8 \mu\text{m}$ up to $1000 \mu\text{m}$, L_{IR} , and the dust mass $M_{\text{dust}} \propto D_L^2 / [\kappa_{\nu} \nu^2 (1+z)]$, where D_L is the luminosity distance, and κ_{ν} is the dust mass absorption coefficient at frequency ν (see Casey 2012 for further details). The fits are presented in Table 2 (see Bitsakis et al. 2011, 2014).

3. A Framework for Group’s Dynamics

Bertschinger (1985) considered self-similar secondary infall and accretion, in an Einstein–de Sitter universe, as an improvement over spherical gravitational collapse (e.g., van de Weygaert & Bond 2008). In this model overdensities decouple from the cosmic expansion at some maximum radius, the first turnaround radius r_{1t} , and then collapse. After crossing, overdensities rebound, but with smaller amplitude, turn around, and recollapse (see CG numerical simulations by Barnes 1985). The pause before the recollapse generates discontinuities in the density and velocity dispersion as functions of radius. Tully (2015, hereafter Tu15) suggested that such discontinuities are observable in the caustic that defines the second turnaround radius r_{2t} . Tully’s insight led to a tight correlation between a group’s line-of-sight velocity dispersion, σ_p , and the projected

second turnaround radius, R_{2t} ,

$$\frac{\sigma_p}{R_{2t}} = (368 \pm 8) h_{75} \text{ km s}^{-1} \text{ Mpc}^{-1}, \quad (1)$$

valid for $70 \leq \sigma_p / \text{km s}^{-1} \leq 1000$, i.e., from galaxies to galaxy clusters, where $\sigma_p = (\sum_i (v_i - \bar{v})^2 / n)^{1/2}$, and \bar{v} is the group’s mean radial velocity, for $i = 1 \dots n$ group members with radial velocities v_i . For spherical symmetry the second turnaround radius is related to the projected turnaround radius $r_{2t} = \sqrt{3/2} R_{2t}$. A direct application of the virial theorem leads to $R_{2t} = 0.215 M_{12}^{1/3} h_{75}^{-2/3} \text{ Mpc}$, where the virial mass $M_v = 2 \times 10^6 (\sigma_p / \text{km s}^{-1})^3 h_{75}^{-1} M_{\odot} = M_{12} \times 10^{12} M_{\odot}$ (see Du08, Section 3). Estimating the first turnaround radius, r_{1t} , requires 3D information to distinguish the decoupling of the infall zone from the Hubble flow. Such information is currently very limited. Nevertheless, Tu15 used direct measurements for Virgo, the M82 group, and the local association (see below), and found an estimate of $r_{1t} = 0.77 M_{12}^{1/3} h_{75}^{-2/3} \text{ Mpc}$. Since both turnaround radii should enclose the same mass, we have $r_{1t} / r_{2t} = 3.14 \pm 0.28$. This ratio is partially justified by theory; see Tu15 for further details.

Using the velocities for H79a, H79b, H79c, H79d, and H79f taken from Du08 and our own measurement using CALIFA data, we find $\bar{v} = 4296 \text{ km s}^{-1}$ and $\sigma_p = 160 \pm 72 \text{ km s}^{-1}$. From Equation (1) we then find $R_{2t} = 435 h_{75}^{-1} \text{ kpc}$, and hence $r_{2t} \approx 533 h_{75}^{-1} \text{ kpc}$, $r_{1t} \approx 1673 h_{75}^{-1} \text{ kpc}$, and $M_v \approx 8.2 \times 10^{12} h_{75}^{-1} M_{\odot}$, i.e., $M_{12} = 8.2$.

Tu15 also introduced *associations* as quasi-virialized regions where giant galaxies along with their respective satellite galaxies are identified as groups. For example, the Milky Way and M31 are defined as two individual groups within the *local association* (see Lynden-Bell 1994). The dynamical history of these galaxy-scale groups could be as complex as in CG—for example, it has been suggested that the dwarf satellite galaxy M32 originates from the disruption of a galaxy comparable to the Milky Way due to an interaction with M31 (D’Souza & Bell 2018).

The Bertschinger secondary infall scenario applies to any overdensity, hence it applies to galaxy-scale groups such as the Milky Way and M31, and to any isolated galaxy halo. In these cases the turnaround radii can be calculated by Equation (1) and the formalism above applies directly. This can be recognized as self-regulated galaxy evolution (e.g., Thomas et al. 2010), as well. Nevertheless, within the current cold dark matter paradigm other effects may be at play, for example, active galactic nucleus (AGN) feedback (e.g., Silk et al. 2014).

Lynden-Bell (1981, 1994, 1999) developed a simple dynamical model for groups of galaxies, in which the solution for the equation of motion can be approximated by the

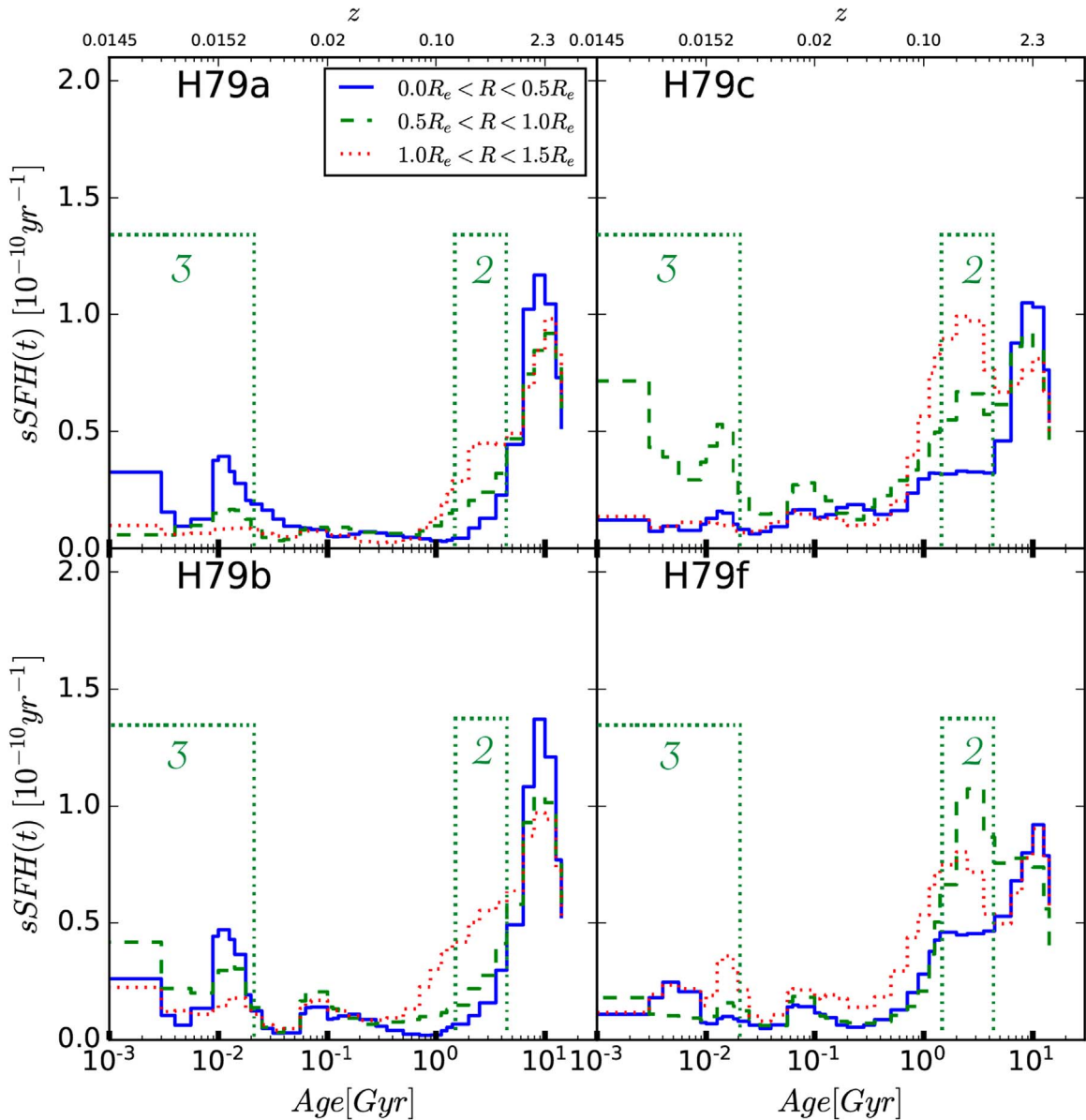


Figure 3. sSFH for SS galaxies. The age of the stellar population, given in Gyr, is indicated on the lower x-axis. The upper x-axis indicates the redshift z , as a proxy for the lookback time. The strength of the sSFH is indicated on the y-axis, expressed in units of $(10^{-10} \text{ yr}^{-1})$. The lines indicate the inner (blue), intermediate (green), and outer (red) regions of the galaxies. The green rectangles labeled 2 and 3 mark coeval episodes of enhanced star formation.

following polynomial (Equation (13) in Lynden-Bell 1994):

$$\left(\frac{GM_{gp}}{r^3}\right)^{\frac{1}{2}}t + 0.85\left(\frac{v}{r}\right)t = 2^{-\frac{3}{2}}\pi \approx 1.11, \quad (2)$$

where G is the gravitational constant, M_{gp} is the total group mass, t is the time, r is the separation between galaxies, and v is the velocity of the galaxies. At the turnaround radius, r_t , the group galaxies are neither approaching nor receding from one another, and so the time of turnaround is given by

$$t = 1.11 \left(\frac{r_t^3}{GM_{gp}}\right)^{\frac{1}{2}}, \quad (3)$$

which is also approximately the freefall time. For a given radius, more massive groups will turn around faster.

If we adopt $M_{gp} = 10 \times 10^{12} M_{\odot}$, then $t_{1t} \sim 11$ Gyr and $t_{2t} \sim 2$ Gyr. Therefore, SS is able to cross at least once within t_H . We suggest that by using the fossil record of star formation of CG galaxies, we can identify the corresponding crossings as tidally induced coeval bursts of star formation. This gives another timing argument to help us constrain the evolution of CG (see Section 4.1).

4. Discussion

4.1. Star Formation History

Great progress in modeling stellar populations has been achieved by the use of extensive stellar libraries, better optimization techniques, and reliable error analysis. It is now possible to trace the evolution of individual galaxies more accurately (e.g., Walcher et al. 2011; Conroy 2013; Ibarra-Medel et al. 2016, 2019; Sánchez et al. 2019). Hence, the

analysis of the sSFH could, in principle, provide us with timing arguments. Hereafter, we assume that group galaxies undergo simultaneous bursts of star formation induced by tidal interaction at each group crossing.

We have restricted our analysis to mass-weighted stellar age. Figure 3 shows the sSFH for H79a, H79b, H79c, and H79f as a function of radius. A smoothing of 0.1 dex was applied to account for the resolution of the stellar libraries.

Figure 3 indicates that the sSFHs of SS galaxies show bursts of star formation at comparable ages but in different regions inside the galaxies. Figure 3 shows that H79f's sSFH is as complex as the other SS galaxies; hence, contrary to Nishiura et al. (2002), we suggest that H79f is a disrupted galaxy rather than a tidal tail (see Du08): H79f's light distribution and low Sérsic index n (see Section 2.2 and Table 1) suggest that H79f was originally a late-type galaxy (see Du08).

A closer examination of Figure 3 suggests that the bursts of star formation in SS galaxies are almost synchronized, with active intervals marked by labeled green rectangles 2 and 3 in the figure. We can test the reality of this synchronization by looking at galaxies not in SS, since we would not expect enhanced SF in the same time intervals. From the CALIFA DR3 database we selected a set of galaxies to serve as a control sample. Since galaxy mass and environment are important drivers of galaxy evolution, we chose galaxies with masses comparable to SS galaxies ($M \sim 10^{10} M_{\odot}$; see Section 4.2) found in groups, pairs, or the field. We also demanded that the selected galaxies should be at redshifts comparable to SS ($z = 0.0145$), to match the age of the SS galaxies and make comparisons easier. The final control sample has 33 galaxies. We found a different sSFH pattern (Figure 4), with no coordinated burst of star formation between any pair of galaxies at any epoch.

Figure 4(a) shows the individual sSFH for control galaxies NGC 3381, NGC 5358, NGC 5402, and UGC 4730. Their histories are representative of typical sSFH patterns that can be found in galaxies of similar mass. Variations in sSFH may be related to the effects of mergers or the assembly of their dark matter halos. We can identify up to three peaks of star formation of varying intensity at different epochs in Figure 4(a). Nevertheless, when we combine the 33 control galaxies, the peaks are smoothed and the pattern of self-regulated star formation emerges, as is apparent in Figure 4(b).

We relate redshift to stellar age (t_{sa} , with $t_{sa} = 0$ in the SS rest-frame, $z_{SS} = 0.0145$), as shown on the upper x -axis of Figure 3. We can identify an initial starburst at $t_{sa} \gtrsim 10$ Gyr ($z \gtrsim 2.3$), which is also seen in the control sample (Figures 4(a), (b)); we label this starburst 1, which is likely of cosmological origin.

Assuming that tidally triggered star formation acts instantaneously, we identify the sSFH peak at stellar age $t_{sa} \sim 3$ Gyr ($z_{fc} \sim 0.3$) with the first crossing, after a first turnaround at $t_{1t} \sim 11$ Gyr. Group-wide interactions at t_{sa} triggered bursts of star formation. This is suggested by the rise of activity in the intermediate and outer regions of each galaxy. H79a and H79b, being more massive, evolve faster, but clear extended star formation is seen in their intermediate and outer regions (green rectangle 2 in Figure 3). This episode of merger-triggered star formation lasted for up to about 3.5 Gyr. Most of the original gas reservoir would have been used during this epoch, and dust would have been largely depleted by starburst-induced winds.

Hence, any later merger would be expected to be dry or mixed (see Bitsakis et al. 2011).

A third peak of star formation is expected after the second turnaround at $t_{2t} \sim 2$ Gyr (see Plauchu-Frayn et al. 2012). There are signs of star formation in the inner regions of H79a and H79b and the intermediate regions of H79c and H79f that peak around $t_{sa} = 0.02$ Gyr (Figure 3); hence, we suggest that SS galaxies began their second crossing at $z_{sc} \sim 0.016$ (green rectangle 3 in the figure). Since a modest level of star formation still continues at $t_{sa} = 0$, we conclude that we are observing SS during its second crossing. This may explain why SS is one of the densest galaxy aggregates known (five galaxies within $37 h_{75}^{-1}$ kpc; see Du08).

The locations of the continuing star formation differ. H79a and H79b show mild star formation in their inner regions, while in H79c only the intermediate region is still forming stars. H79f has lost most of its gas so that only a low level of star formation can be sustained. Figures 4 and 5 show that SS follows a different pattern of star formation than the control galaxies. The second burst of star formation happened slightly earlier than in the control sample on average. However, the most noticeable difference is seen at redshifts around $z = 0.0145$, where the control galaxies show a monotonic decline of their mean sSFH.

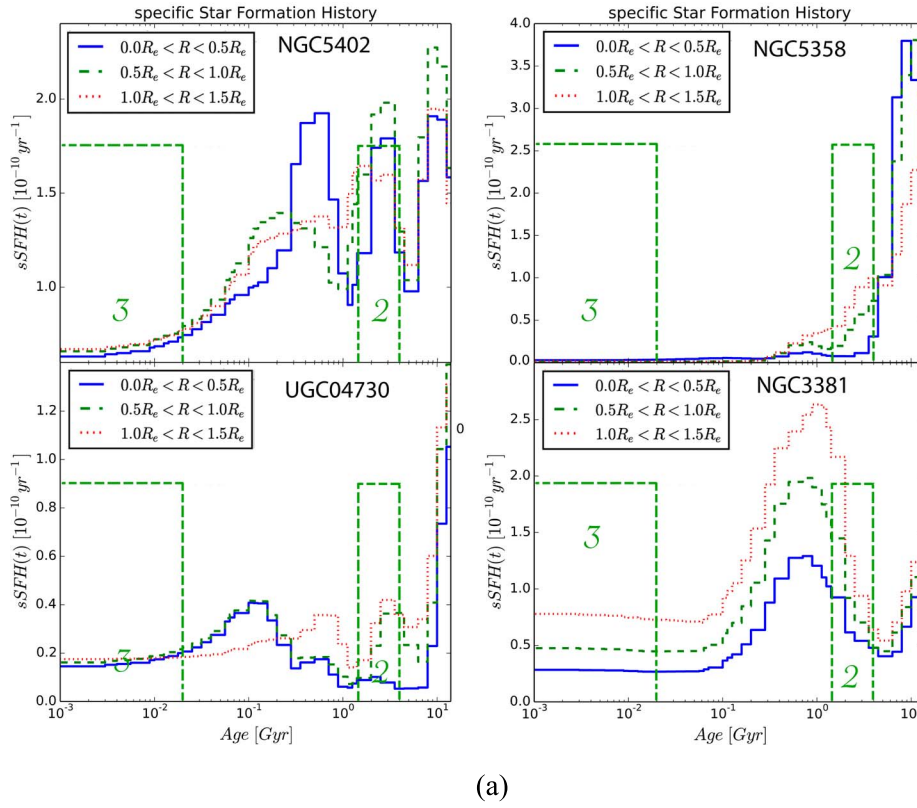
To complete our scenario, we propose that during each crossing some galaxies might be disrupted (e.g., H79f), losing their stars and gas to enrich the intragroup medium (see Da Rocha & Mendes de Oliveira 2005; Borthakur et al. 2010; Zemcov et al. 2014).

Since SS galaxies have appreciable sSFR at present (Figure 3, region 3) we should be able to detect the spectral signature of star formation. Figure 1 indeed shows that the spectra of the SS galaxies have broad absorption Balmer lines resembling post-starburst galaxies. This indicates an episode of star formation less than 1 Gyr old (Pawlik et al. 2018 and references therein). After the modeling in Section 2.3 and removing the emission of ionized gas, we determine the equivalent widths (EW_{λ}) of $H\alpha$ to be $EW(H\alpha) = 2.2 \pm 0.5 \text{ \AA}$, $EW(H\alpha) = 2.3 \pm 0.2 \text{ \AA}$, $EW(H\alpha) = 2.9 \pm 0.4 \text{ \AA}$, and $EW(H\alpha) = 3.2 \pm 0.9 \text{ \AA}$ in H79a, H79b, H79c, and H79f, respectively. These values are the same, to within the errors. Balmer lines are prominent in B and A stars, whose main-sequence lifetime ($t_{ms} \sim 10^{10}(M_{*}/M_{\odot})^{-2.5}$, where M_{*} is the mass for an upper main-sequence star; Hansen & Kawaler 1994, p.28) runs between 0.1 and 1 Gyr, consistent with the ages enclosed by region 3 in Figure 3 where a low level of star formation continues. The similarity of the EW for the SS galaxies supports the idea of a recent common history of star formation associated with the dynamical evolution of the group.

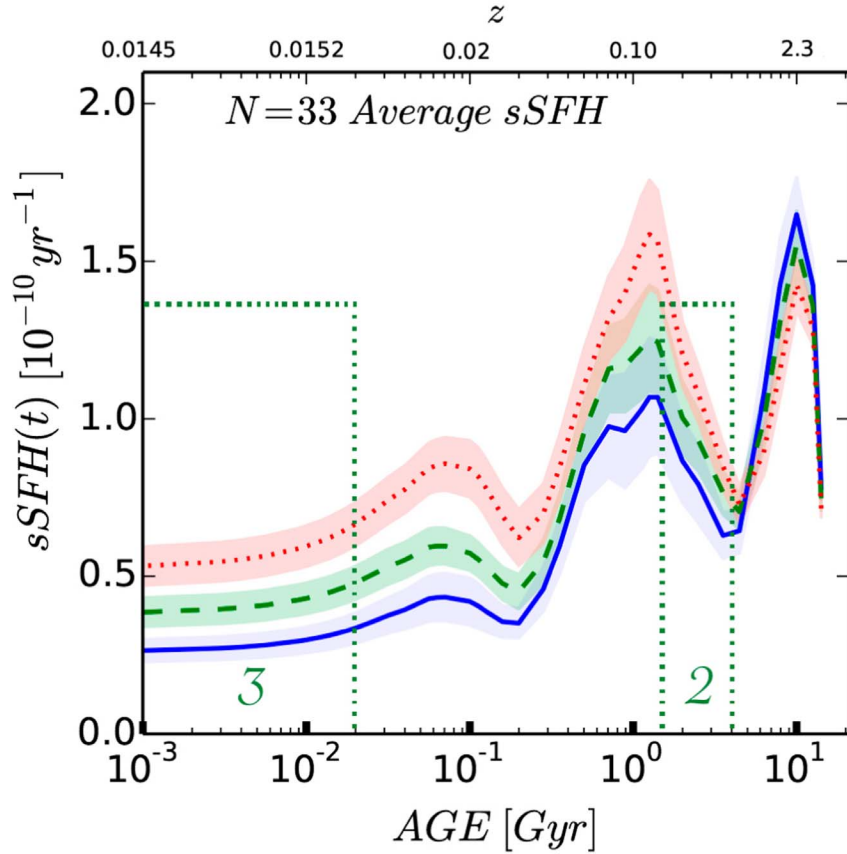
There is an important caveat to the qualitative analysis of the sSFH presented above. The sSFH obtained in Section 4.1 depends strongly on the adopted SSP library and the details of the inversion method (e.g., Cid Fernandes et al. 2014; Sánchez et al. 2019). Therefore, our results although consistent and suggestive, remain quantitatively strongly model-dependent.

4.2. Kinematics in H79b

We analyzed the kinematics of H79b using techniques developed by Barrera-Ballesteros et al. (2014) and García-Lorenzo et al. (2015). Kinematic centers for the stellar and ionized-gas components were generated via gradient maps from the velocity fields shown in Figure 5(a). Figure 5(b)



(a)



(b)

Figure 4. (a) sSFH for the control galaxies NGC 3381, NGC 5358, NGC 5402, and UGC 4730. (b) The average sSFH for 33 control galaxies of similar mass and redshift as SS galaxies. All data have been taken from the CALIFA sample. The notation is the same as in Figure 3.

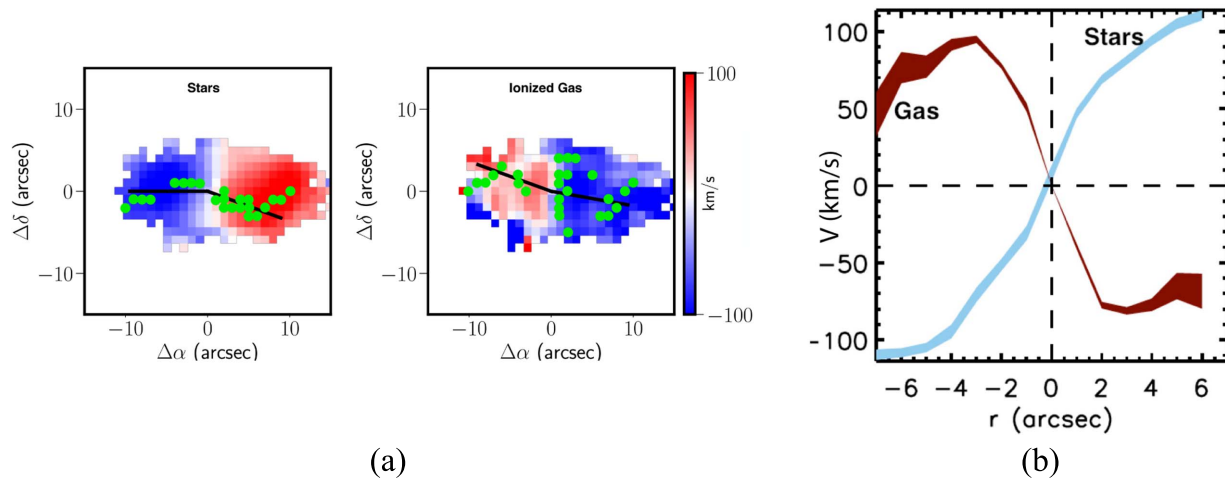


Figure 5. Counter-rotating disk in H79b. (a) The velocity fields due to stars and ionized gas, respectively. In each panel, green points highlight the radii of maximum velocities, determined from the pseudo-rotation curves (pRC) of H79b. Black lines represent the average kinematic PA. The color-coded velocity scale is shown on the right. (b) The pRCs for the stars (blue) and ionized gas (brown).

shows the pseudo-rotation curves (pRCs; Barrera-Ballesteros et al. 2014) for the stellar and ionized-gas components. The amplitudes of the pRCs are similar but counter-rotating. The maximum stellar rotation speed in Figure 5(b), $v_{\max} \simeq 110 \text{ km s}^{-1}$, leads to a dynamical mass $M_{\text{dyn}}(r) = 1.8 r G^{-1}(0.5v_{\max}^2 + \sigma_{\text{gal}}^2)$ (Aquino-Ortíz et al. 2018, Equation (5), Section 5.2) for H79b within $r = R_e$, where $\sigma_{\text{gal}} = 145 \text{ km s}^{-1}$ is the velocity dispersion, so that $M_{\text{dyn}}(R_e) \simeq 2 \times 10^{10} M_{\odot}$ (see Du08).

We interpret the counter-rotating disk in H79b as evidence for multiple encounters with other galaxies and gas removal followed by reaccretion from the intragroup medium. The numerical simulations of Starkenburg et al. (2019) support such an origin for counter-rotating disks in dense environments. Starkenburg et al. also estimated that counter-rotating disks could remain stable for 2 Gyr or more. Therefore, we propose that the counter-rotating disk in H79b was created during the first crossing (region 2 in Figure 3).

4.3. The Distribution of Ionized Gas

Figure 2(b) maps the distribution of H α in emission above a conservative flux cut of $1.2 \times 10^{-16} \text{ erg s}^{-1} \text{ cm}^{-2} \text{ arcsec}^{-2}$. The ionized gas concentrates toward the galaxy nuclei. H79c shows only faint emission, while H79f has only fainter emission. The pattern shown by the IFU data agrees with Fabry-Pérot observations by Du08.

Line ratios useful for diagnostic diagrams were measured with uncertainties calculated by propagating the errors in quadrature. Different classification criteria (Kewley et al. 2001, 2006; Kauffmann et al. 2003; Stasińska et al. 2006; Schawinski et al. 2007) are overplotted in Figure 6, where the spaxel radial distribution, scaled by R_e , is indicated by the color bar. The distribution for H79a (upright colored triangles) shows some AGN/LINER activity, while H79b is dominated by composite activity (colored circles), though star formation driven by galaxy-galaxy interactions (e.g., Hopkins et al. 2009) is seen close to the nuclei. Nevertheless, no region within the H79a/H79b envelope has starburst characteristics.

The comparison of Figure 6 in this Letter with Figure 6 in Sánchez et al. (2015) suggests that the underlying stellar populations of H79a and H79b are old (i.e., with luminosity-weighted age $\gtrsim 10^{9.5}$ yr), but prolonged star formation activity over the last several Myr might be present (e.g., Coenda et al. 2015; Sánchez et al. 2015).

The results of this subsection are in agreement with Section 4.1, as we expected only a low level of star formation in the SS galaxy central regions. Moreover, the comparison of our diagnostic diagrams with earlier results suggest that the underlying stellar population is old.

There are indications of biconical outflows in galaxies H79a and H79b, but we leave the hydrodynamical analysis of the ionized gas for a further publication.

4.4. Star Formation Derived from IR Observations

An independent indicator of star formation is provided by IR properties. We coadded the pure gas spectra (Section 2.3) across H79b to derive $L_{\text{H}\alpha} = (4 \pm 1) \times 10^{40} \text{ erg s}^{-1}$, which leads to the estimate $\text{SFR}_{\text{H}\alpha} = (7.9 \times 10^{-42}) \times L_{\text{H}\alpha} = 0.3 \pm 0.1 M_{\odot} \text{ yr}^{-1}$ (Kennicutt 1998). Using the IR luminosity (Section 2.5), we get $\text{SFR}_{\text{IR}} = 1.71 \times 10^{-10} L_{\text{IR}} = 0.5 \pm 0.1 M_{\odot} \text{ yr}^{-1}$ (Kennicutt 1998). Although the inferred SFR from the dust emissivity is only accurate to 10% (Casey 2012), it is encouraging that the two estimates are in fair agreement. The H α emission is not completely sampled across H79a and is low in H79c; hence, we have only calculated the SFR for these galaxies based on the IR scaling law. We found $\text{SFR}_{\text{IR}} = 0.64 \pm 0.06 M_{\odot} \text{ yr}^{-1}$ and $0.07 \pm 0.02 M_{\odot} \text{ yr}^{-1}$, for H79a and H79c, respectively. Our SFRs are close to the results of Bitsakis et al. (2011), but are an order of magnitude higher than Bitsakis et al. (2014)—it is known that cmcircsd underestimates M_{dust} compared with the more detailed modeling provided by MAGPHYS over a much wider spectral range (Bitsakis et al. 2014). Overall, the discrepancies among the estimated parameters can be accounted for by the differences in the definition of SFR and

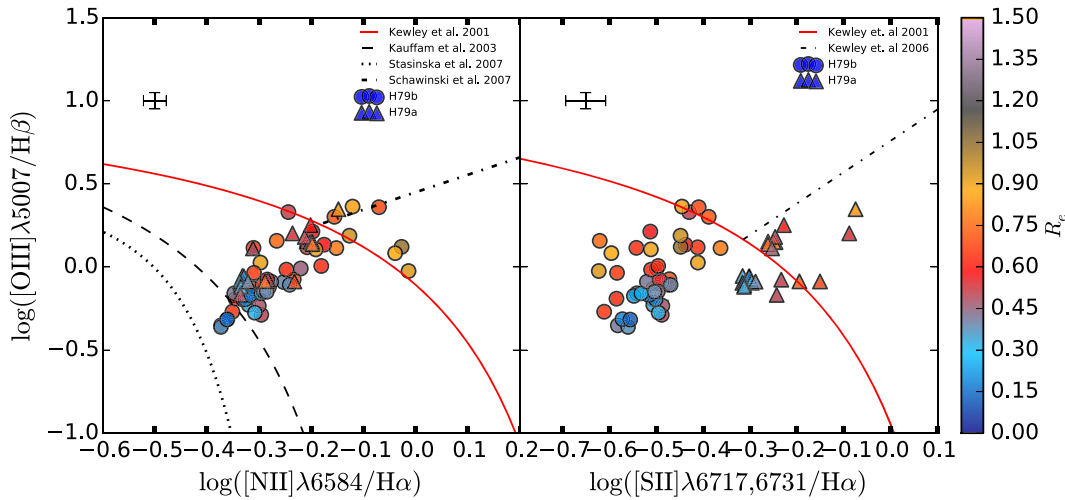


Figure 6. Line-ratio diagnostic diagrams given by spaxel as a function of distance to the center scaled by the effective radius (R_e) for H79a (upright triangles) and H79b (circles). Mean errors are indicated on the upper left. The overplotted black lines represent empirically or theoretically derived diagnostics for LINER/Seyfert and star formation activity. No spaxel shows starburst activity.

dust attenuation employed in the modeling (e.g., Hung et al. 2016; Hunt et al. 2019) and the assumed cosmology.

Despite the discrepancies cited above, we conclude that star formation in H79a, H79b, H79c, and H79f is presently low (see Sections 4.1, 4.3).

The HI distribution over SS also supports the low level of star formation suggested above. HI is not scattered over the whole group; it is actually centered on H79d, showing weak emission extending to the east and northeast, which might suggest that H79d is entering SS for the first time (e.g., Du08). However, HI is deficient corresponding to 30%–70% of the expected HI for the optical luminosities and morphological types (Verdes-Montenegro et al. 2001; Borthakur et al. 2010). In this work, we suggest that SS is going through its second crossing; hence, the observed HI deficiency resulted because it might have been exhausted during the first crossing (Section 4.1).

5. Conclusions

1. The analysis presented above allows us to reject the ideas that SS is a chance projection or assembling for the first time: we suggest that SS is experiencing secondary infall. The underlying stellar population is old and current star formation is low (Sections 4.1, 4.3). The distribution of morphologies and the compactness of SS galaxies (Section 2.2), the presence of a disrupted galaxy (H79f, Section 4.1), displaced HI (e.g., Du08, Borthakur et al. 2010), and luminous intragroup light are suggestive of strong interactions.
2. Using a simple dynamical framework based on secondary infall in Section 3 we have been able to calculate the first and second turnaround radii for SS. We found $r_{1t} \approx 1670 h_{75}^{-1}$ kpc and $r_{2t} \approx 530 h_{75}^{-1}$ kpc. We also derived a virial mass $M_v \approx 8.2 \times 10^{12} h_{75}^{-1} M_\odot$. Since CGs are neither expanding nor contracting at the turnaround radius, we can calculate the corresponding freefall times, and find $t_{1t} \sim 11$ Gyr and $t_{2t} \sim 2$ Gyr. Hence, SS is able to cross at least once during a Hubble time.
3. We suggest that by using the fossil record of star formation of CG galaxies (Sections 2.3, 4.1), we can

identify the corresponding crossings with tidally induced coeval bursts of star formation. We generated the sSFHs of the SS galaxies over three ranges of radii using PIPE3D, and found coordinated episodes of star formation in H79a, H79b, H79c, and H79f that are not present in a control sample. Our qualitative analysis allow us to identify three episodes of star formation. The first, at stellar age $t_{sa} \gtrsim 10$ Gyr ($z \gtrsim 2.3$), corresponds to the formation of each galaxy. The second episode times the first crossing to stellar age $t_{sa} \sim 3$ Gyr ($z_{fc} \sim 0.3$) and lasted for about 3.5 Gyr. We found an ongoing episode of mild star formation at $t_{sa} = 0.02$ Gyr, from which we suggest that the SS galaxies began their second crossing around $z_{sc} \sim 0.016$. This may be the origin of the extreme compactness of SS.

4. The presence and stability (for more than $\gtrsim 2$ Gyr) of a counter-rotating disk in H79b provides an independent timing for the first crossing (Section 4.2).
5. The integrated spectra of H79a, H79b, H79c, and H79f resemble those of post-starburst galaxies (Figure 1). This is indicative of a recent episode of star formation not more than 1 Gyr ago. A recent coordinated episode of star formation would result in strong Balmer lines having the same EW. Indeed, we found that the four galaxies have an EW ~ 2.6 Å in H α (Section 4.1). This episode of star formation could be 0.1–1 Gyr old, giving another bound on the time of the second crossing, independent of the adopted stellar population model.
6. The analysis of diagnostic diagrams (Section 4.3) and the IR emission (Section 4.4) of SS galaxies suggests that star formation is currently at a low level throughout the group.
7. The complex history of galaxy interactions suggested by our dynamical model (Section 3) and the fossil record (Section 4.1) explains why mergers in CGs are dry or mixed and the origin and enrichment of the intragroup medium.
8. The techniques and dynamical scenario used in this Letter may help to explore the assembly of groups and clusters of galaxies.
9. The scenario that we have advanced in this Letter provides a plausible solution to the short crossing time


paradox in CGs, and may serve to constrain other models (e.g., Athanassoula et al. 1997; Tamayo & Aceves 2017).

We acknowledge the careful revision of our Letter and most relevant suggestions of an anonymous referee, which helped us to greatly improve the results and discussions presented above. We are very grateful to Prof. Frederic A. Rasio, the Letters Editor, for allowing us to exceed the nominal length limits to answer to the referee's remarks and suggestions. O.L.-C. is grateful to the Department of Astronomy and Astrophysics of the University of North Dakota for appointing him the 2015-2016 Oliver L. Benediktson Endowed Chair in Astrophysics, during such appointment the core of this Letter was developed. O.L.-C. acknowledges enlightening discussions with Marina Rodríguez-Baras, Luis Aguilar, Josh Barnes, Theo Bitsakis, Héctor Aceves, and Gustavo Bruzual. S.F.S. thanks PAPIIT-DGAPA-IN100519, Conacyt CB-285080, and FC-2016-01-1916 projects. This study uses data from the CALIFA survey.¹⁹ Based on observations collected at CAHA, operated jointly by MPIA and IAA (CSIC).


Facilities: CAO:3.5 (PMAS, PPak), *HST* (WFPC2), *WISE*.

ORCID iDs

Omar López-Cruz  <https://orcid.org/0000-0002-1381-7437>

Héctor Javier Ibarra-Medel  <https://orcid.org/0000-0002-9790-6313>

Mark Birkinshaw  <https://orcid.org/0000-0002-1858-277X>

Jorge K. Barrera-Ballesteros  <https://orcid.org/0000-0003-2405-7258>

Jesús Falcon-Barroso  <https://orcid.org/0000-0002-0608-9574>

Wayne A. Barkhouse  <https://orcid.org/0000-0001-5547-3938>

Juan P. Torres-Papaqui  <https://orcid.org/0000-0002-8009-0637>

References

- Aquino-Ortiz, E., Valenzuela, O., Sánchez, S. F., et al. 2018, *MNRAS*, **479**, 2133
- Athanassoula, E., Makino, J., & Bosma, A. 1997, *MNRAS*, **286**, 825
- Barnes, J. 1985, *MNRAS*, **215**, 517
- Barnes, J. E. 1997, in ASP Conf. Ser. 116, The Nature of Elliptical Galaxies, ed. M. Arnaboldi, G. S. Da Costa, & P. Saha (San Francisco, CA: ASP), 469
- Barrera-Ballesteros, J. K., Falcón-Barroso, J., García-Lorenzo, B., et al. 2014, *A&A*, **568**, A70
- Bertschinger, E. 1985, *ApJS*, **58**, 39
- Bitsakis, T., Charmandaris, V., Appleton, P. N., et al. 2014, *A&A*, **565**, A25
- Bitsakis, T., Charmandaris, V., da Cunha, E., et al. 2011, *A&A*, **533**, A142
- Borthakur, S., Yun, M. S., & Verdes-Montenegro, L. 2010, *ApJ*, **710**, 385
- Cappellari, M., & Emsellem, E. 2004, *PASP*, **116**, 138
- Cardelli, J. A., Clayton, G. C., & Mathis, J. S. 1989, *ApJ*, **345**, 245
- Casey, C. M. 2012, *MNRAS*, **425**, 3094
- Cid Fernandes, R., González Delgado, R. M., García Benito, R., et al. 2014, *A&A*, **561**, A130
- Cid Fernandes, R., Lacerda, E. A. D., González Delgado, R. M., et al. 2015, in IAU Symp. 309, Galaxies in 3D Across the Universe, ed. B. L. Ziegler et al. (Cambridge: Cambridge Univ. Press), 93
- Cid Fernandes, R., Mateus, A., Sodré, L., Stasińska, G., & Gomes, J. M. 2005, *MNRAS*, **358**, 363
- Coenda, V., Muriel, H., & Martínez, H. J. 2015, *A&A*, **573**, A96
- Conroy, C. 2013, *ARA&A*, **51**, 393
- Courteau, S., Cappellari, M., de Jong, R. S., et al. 2014, *RvMP*, **86**, 47
- Da Rocha, C., & Mendes de Oliveira, C. 2005, *MNRAS*, **364**, 1069
- D'Souza, R., & Bell, E. F. 2018, *NatAs*, **2**, 737
- Diaferio, A., Ramella, M., Geller, M. J., & Ferrari, A. 1993, *AJ*, **105**, 2035
- Díaz-Giménez, E., & Zandivarez, A. 2015, *A&A*, **578**, A61
- Durbala, A., del Olmo, A., Yun, M. S., et al. 2008, *AJ*, **135**, 130
- García-Benito, R., Zibetti, S., Sánchez, S. F., et al. 2015, *A&A*, **576**, A135
- García-Lorenzo, B., Márquez, I., Barrera-Ballesteros, J. K., et al. 2015, *A&A*, **573**, A59
- González Delgado, R. M., Cid Fernandes, R., García-Benito, R., et al. 2014, *ApJL*, **791**, L16
- Hansen, C. J., & Kawaler, S. D. 1994, Stellar Interiors, Physical Principles, Structure, and Evolution (New York: Springer)
- Hickson, P. 1993, *ApL&C*, **29**, 1
- Hopkins, P. F., Cox, T. J., Younger, J. D., & Hernquist, L. 2009, *ApJ*, **691**, 1168
- Hung, C.-L., Casey, C. M., Chiang, Y.-K., et al. 2016, *ApJ*, **826**, 130
- Hunt, L. K., De Looze, I., Boquien, M., et al. 2019, *A&A*, **621**, A51
- Ibarra-Medel, H. J., Avila-Reese, V., Sánchez, S. F., et al. 2019, *MNRAS*, **483**, 4525
- Ibarra-Medel, H. J., Sánchez, S. F., Avila-Reese, V., et al. 2016, *MNRAS*, **463**, 2799
- Kauffmann, G., Heckman, T. M., Tremonti, C., et al. 2003, *MNRAS*, **346**, 1055
- Kelz, A., Verheijen, M. A. W., Roth, M. M., et al. 2006, *PASP*, **118**, 129
- Kennicutt, R. C., Jr. 1998, *ARA&A*, **36**, 189
- Kewley, L. J., Dopita, M. A., Sutherland, R. S., Heisler, C. A., & Trevena, J. 2001, *ApJ*, **556**, 121
- Kewley, L. J., Groves, B., Kauffmann, G., & Heckman, T. 2006, *MNRAS*, **372**, 961
- Lynden-Bell, D. 1981, *Obs*, **101**, 111
- Lynden-Bell, D. 1994, in Proc. 5th Canary Islands Winter School of Astrophysics, The Formation and Evolution of Galaxies, ed. C. Muñoz-Tuñón & F. Sánchez (Cambridge: Cambridge Univ. Press), 85
- Lynden-Bell, D. 1999, in IAU Symp. 192, The Stellar Content of Local Group Galaxies, ed. P. Whitelock & R. Cannon (San Francisco, CA: ASP), 39
- Nishiura, S., Shioya, Y., Murayama, T., et al. 2002, *PASJ*, **54**, 21
- Pawlik, M. M., Taj Aldeen, L., Wild, V., et al. 2018, *MNRAS*, **477**, 1708
- Peebles, P. J. E. 1971, Physical Cosmology (Princeton, NJ: Princeton Univ. Press), 83
- Peng, C. Y., Ho, L. C., Impey, C. D., & Rix, H.-W. 2010, *AJ*, **139**, 2097
- Pérez, E., Cid Fernandes, R., González Delgado, R. M., et al. 2013, *ApJL*, **764**, L1
- Plauchu-Frayn, I., Del Olmo, A., Coziol, R., et al. 2012, *A&A*, **546**, A48
- Roth, M. M., Kelz, A., Fechner, T., et al. 2005, *PASP*, **117**, 620
- Sánchez, S. F., Avila-Reese, V., Rodríguez-Puebla, A., et al. 2019, *MNRAS*, **482**, 1557
- Sánchez, S. F., García-Benito, R., Zibetti, S., et al. 2016, *A&A*, **594**, A36
- Sánchez, S. F., Pérez, E., Rosales-Ortega, F. F., et al. 2015, *A&A*, **574**, A47
- Sánchez, S. F., Pérez, E., Sánchez-Blázquez, P., et al. 2016a, *RMxAA*, **52**, 21
- Sánchez, S. F., Pérez, E., Sánchez-Blázquez, P., et al. 2016b, *RMxAA*, **52**, 171
- Schawinski, K., Thomas, D., Sarzi, M., et al. 2007, *MNRAS*, **382**, 1415
- Schlegel, D. J., Finkbeiner, D. P., & Davis, M. 1998, *ApJ*, **500**, 525
- Seyfert, C. K. 1951, *PASP*, **63**, 72
- Silk, J., Di Cintio, A., & Dvorkin, I. 2014, in Galaxy Formation, Post-Planck Cosmology, Ecole de Physique des Houches, ed. B. Wandelt et al. (Oxford: Oxford Univ. Press), 137
- Starkenbug, T. K., Sales, L. V., Genel, S., et al. 2019, arXiv:1903.03627
- Stasińska, G., Cid Fernandes, R., Mateus, A., Sodré, L., & Asari, N. V. 2006, *MNRAS*, **371**, 972
- Tamayo, F. J., & Aceves, H. 2017, *RMxAA*, **53**, 515
- Thomas, D., Maraston, C., Schawinski, K., et al. 2010, *MNRAS*, **404**, 1775
- Tully, R. B. 2015, *AJ*, **149**, 54
- van de Weygaert, R., & Bond, J. R. 2008, *LNP*, **740**, 335
- Verdes-Montenegro, L., Yun, M. S., Williams, B. A., et al. 2001, *A&A*, **377**, 812
- Walcher, J., Groves, B., Budavári, T., et al. 2011, *Ap&SS*, **331**, 1
- White, S. D. M. 1990, in Dynamics and Interactions of Galaxies, ed. R. Wielen (Berlin: Springer), 380
- Zemcov, M., Smidt, J., Arai, T., et al. 2014, *Sci*, **346**, 732

¹⁹ <http://califa.caha.es/>